RESEARCH ARTICLE

WILEY

A phase-field formulation based on an extended F-criterion for rock fracture

Pan Sun[1,2] | Zhitang Lu[3] | Zhiliang Wang[1] | Jie Wu[4]

[1]College of Civil & Hydraulic Engineering, Hefei University of Technology, Hefei, China

[2]Anhui Key Laboratory of Civil Engineering Structures and Materials, Hefei University of Technology, Hefei, China

[3]School of Resources and Environmental Engineering, Hefei University of Technology, Hefei, China

[4]Key Laboratory for Mechanics in Fluid Solid Coupling Systems, Institute of Mechanics, Chinese Academy of Sciences, Beijing, China

Correspondence
Jie Wu, Key Laboratory for Mechanics in Fluid Solid Coupling Systems, Institute of Mechanics, Chinese Academy of Sciences, Beijing, China.
Email: jie.voo@gmail.com

Funding information
Natural Science Foundation of Hebei Province, Grant/Award Number: D2019202440; National Natural Science Foundation of China, Grant/Award Numbers: 41807277, 42172306

Abstract

In this paper a phase-field formulation based on an extended F-criterion (the normalized strain energy release rate criterion) is proposed to simulate tensile-compressive-shear rock fractures. By applying the F-criterion, the phase-field crack-driving energy decomposition is determined by a direction search which maximizes the local fracture dissipation. In compressive-shear states, the computation is supplemented by an explicitly expressed confinement-dependent mode-II fracture energy release rate, and the cracking angle is determined by both the fracture energy and strain states. The hybrid formulation and alternate minimization algorithm are adopted for the numerical examples in this paper. Fractures for rock and rock-like specimens subjected to compression demonstrate the ability of the present model in capturing tensile-compressive-shear rock fracture behaviors.

KEYWORDS
compressive-shear fracture, directional decomposition, phase-field, rock fracture

1 | INTRODUCTION

During uniaxial and biaxial compression tests, rock may exhibit a combination of flaw slippage, onset, and propagation of wing and secondary cracks, and coalescence and branching of these cracks, depending on material properties and stress states. Capturing such failure mechanisms faithfully in a numerical model is, nevertheless, not a trivial task. In recent years, the phase-field model has emerged as an elegant and attractive method for fracture initiation, propagation, and coalescence simulation. Originated from the Griffith's theory,[1] the phase-field model has now been applied to brittle fracture,[2,3] quasi-brittle fracture,[4–6] dynamic fracture,[7–9] ductile fracture,[10–13] thermo-mechanical-driven fracture,[14,15] hydro-fracture,[16,17] and so on.

In examining rock fracture, numerous efforts have been made for phase-field models to adapt to fracturing characteristics of rock, including the compressive-shear fracture and the difference in mode-I and mode-II fracture energies. The sphere-deviatoric split[18] and spectral split[19] proposed in the classical phase-field models to prevent damage under compression alone are unable to capture these complex phenomena. Zhang et al.[20] was the first to normalize the contribution of mode-I and mode-II crack driving energy by the corresponding critical fracture energy based on the modified maximum

energy release rate criterion, or the so-called F-criterion.[21] Their work successfully reproduces classical experimental tests for rock-like specimens with a single flaw and double flaws under compression. Liu et al.[22] used volumetric-deviatoric split, the Benzaggagh-Kenane failure criterion for mixed-mode fracture and non-isotropic degradation function to capture complex rock fracture features. To consider the effect of cohesion and internal friction angle on rock strength and inspired by the macroscopic Mohr-Coulomb strength criterion, Zhou et al.[23] and Xu et al.[24] proposed a cracking driving energy formulated by the over shear force based on the Mohr-Coulomb strength criterion. Similarly, Jia et al.[25] proposed an over-shear formulation for cracking driving energy based on the Hoek-Brown strength criterion.

The aforementioned work generally does not consider the direction of the regularized smeared crack. Strobl and Seelig[26] was the first to notice the problem of an isotropic degradation of stiffness when the crack is fully developed, and proposed to decompose the strain taking crack orientations into account. Bryant and Sun[27] later used a different approach for energy decomposition by locally searching the maximum energy dissipation direction. The local energy minimization is also based on the F-criterion. Wang et al.[28,29] proposed a universal fracture criterion in phase-field models for tensile-compressive-shear fracture. In their formulation, the crack direction is determined by a local maximation of normalized stress. Steinke and Kaliske[30] proposed a directional stress decomposition to derive a proper crack driving strain energy term which fulfills basic crack characteristics defined for ideal plane and frictionless crack surfaces. Fan et al.[31] developed a directional splitting method for mixed-mode fracture in which the local crack coordinate system is determined by the F-criterion and a quasi-monolithic algorithm is used therein. Their stress split for the mode-I fracture can find its origin in the work by Freddi and Royer-Carfagni[32] for the phase-field model and by Wu and Cervera[33] for continuum damage mechanics (CDM) model. To consider energy consumption by the frictional force on the closed sliding surface, Fei and Choo[34,35] proposed a unique stress-decomposition scheme in phase-field models for pressure-sensitive geomaterials. In their model, the cracking direction is the same as that obtained from the macroscopic Mohr–Coulomb strength theory. To accurately simulate material behaviors in the post-fracture stage, Luo et al.[36] presented a phase-field model with a directional strain decomposition to consider the crack surface normal and a stress-driven crack opening indicator to distinguish the opening and closure of pre-cracks. Steinke et al.[37] discussed in detail the spatial orientation of the potential crack surface and the issue of internal locking and lateral phase-field evolution due to local orientation misalignment.

As stated by many researchers, the shear fracture energy of rock is dependent on the confining pressure. Backers et al.[38,39] found Mode-II fracture toughness increases for limestone, marble, and granite with increasing confining pressure until a plateau is reached when the confining pressure exceeds 30 MPa. Choo et al.[40] investigated experimental data in the literature for stiff clays and shales, and established an empirical power equation between rock shear fracture energy and confining pressure. Zhang et al.[41] performed confined rock fracture tests on short core in compression (SCC) specimens, which show a linear increase of the mode-II fracture toughness with confining pressure in the range of 0–35 MPa, and its value exhibited at 35 MPa confining pressure is two to three times higher than that at atmospheric pressure. Wu et al.[42] performed particle flow code (PFC) simulations for punch-through shear tests and obtained similar confinement-related shear fracture energy increasing behavior, which is consistent with Backers' findings.

As mentioned by Backers et al.,[38] the confinement effect is most likely related to the friction effect of rock. It is interesting to note that this property is considered in deriving the crack driving energy term in phase-field models by a subtraction of internal friction force in the work of Zhou et al.[23] and Fei and Choo.[43] In this paper, the friction effect is considered in an alternative way by using an explicit expression of shear fracture energy dependence on the normal stress. Furthermore, the cracking angle is solved locally by using the F-criterion to obtain the corresponding crack driving energy, which is the main novelty of this work and fundamental for future contact simulation of rock blocks.

This paper is organized as follows. In Section 2, the phase-field formulation based on an extended F-criterion for rock fracture is detailed. In Section 3, the implementation aspects are shortly introduced followed by numerical examples in Section 4. Section 5 concludes this paper.

2 | PHASE-FIELD FORMULATION BASED ON AN EXTENDED F-CRITERION

2.1 | Crack topology regularization and variational principle

In phase-field models, a discrete crack surface Γ (Figure 1) is regularized by a crack surface density function $\gamma(d, \nabla d)$ as

$$\gamma\left(d, \nabla d\right) = \frac{1}{c_0}\left(\frac{1}{l_0}\alpha\left(d\right) + l_0(\nabla d)^2\right) \text{ with } c_0 = 4\int_0^1 \sqrt{\alpha\left(\beta\right)}d\beta \tag{1}$$
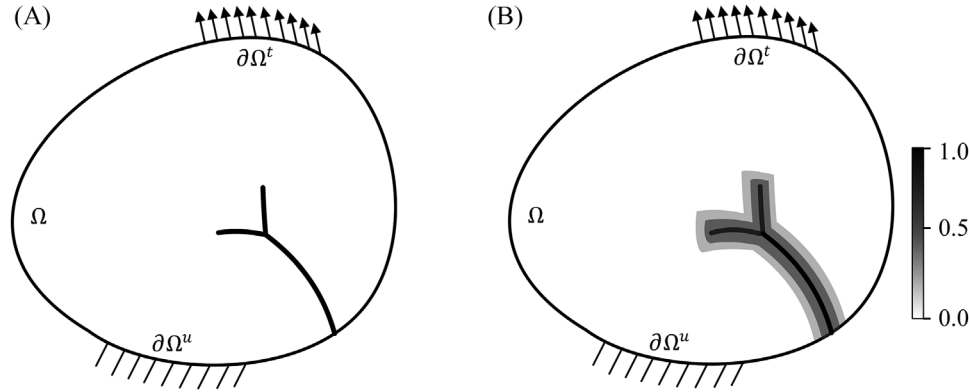
FIGURE 1 Crack topology regularization in phase-field models: (A) discrete crack; (B) regularized crack.

d is the phase-field variable and ∇d is its gradient. The classical AT1, AT2 and PF-CZM[44] models use, respectively

$$\alpha\,(d) = \begin{cases} d, & \textit{AT1 model} \\ d^2, & \textit{AT2 model} \\ 2d - d^2, & \textit{PF} - \textit{CZM} \end{cases}, \text{ and } c_0 = \begin{cases} 8/3, & \textit{AT1 model} \\ 2, & \textit{AT2 model} \\ \pi, & \textit{PF} - \textit{CZM} \end{cases} \tag{2}$$

In this paper, the AT2 model is used. The energetic degradation function is defined upon d and the most generic form is the quadratic one, which reads

$$g\,(d) = (1 - d)^2 \tag{3}$$

Then, the free energy of a cracked body is written as

$$\Pi \;=\; \int_\Omega g\,(d)\,\psi_0\,(\nabla^s u)\,\mathrm{d}\Omega + \smallint_\Omega G_c \gamma\,(d, \nabla d)\,\mathrm{d}\Omega - \int_\Omega f^{\mathrm{T}} \cdot u\mathrm{d}\Omega - \smallint_{\partial\Omega^t} t^{\mathrm{T}} \cdot u\mathrm{d}S \tag{4}$$

where $\psi_0(\nabla^s u)$ is the elastic energy density for undamaged materials, G_c is the critical energy release rate, f is the body force, and t is the traction. Using the minimization of the total energy leads to the following strong form for the displacement field and phase field

$$\begin{cases} \nabla \cdot \sigma + f \;=\; 0 \\ \sigma \cdot n \;=\; t^* \;\; on\; \partial\Omega^t \\ u \;=\; u^* \;\; (on)\; \partial\Omega^u \end{cases} \tag{5}$$

$$\begin{cases} 2\,(1 - d)\dfrac{\mathcal{H}}{G_c} - \dfrac{d}{l_0} + l_0 \Delta d \;=\; 0 \\ \nabla d \cdot n \;=\; 0 \;\; on\; \partial\Omega \end{cases} \tag{6}$$

σ is the stress tensor and n is the outward normal to the traction boundary $\partial\Omega^t$. In Equation (6), a history variable $\mathcal{H}$ recording the maximum ψ_0 reached in the loading history is used to prevent crack healing. Further, to distinguish the difference of rock in mode-I and mode-II critical energy release rate, Zhang et al.[20] proposed to replace $\dfrac{\mathcal{H}}{G_C}$ term in driving phase field propagation in Equation (6) with $\dfrac{\mathcal{H}_{\mathrm{I}}}{G_{\mathrm{Ic}}} + \dfrac{\mathcal{H}_{\mathrm{II}}}{G_{\mathrm{IIc}}}$, where $\mathcal{H}_{\mathrm{I}}$ and $\mathcal{H}_{\mathrm{II}}$ are history variables, respectively, contributed by volume dilation and shear deformation as

$$\mathcal{H}_{\mathrm{I}} = \lambda \left\langle tr\,[\varepsilon] \right\rangle_+^2, \;\; \mathcal{H}_{\mathrm{II}} = \mu tr \left[\left\langle \varepsilon \right\rangle_+^2 \right] \tag{7}$$
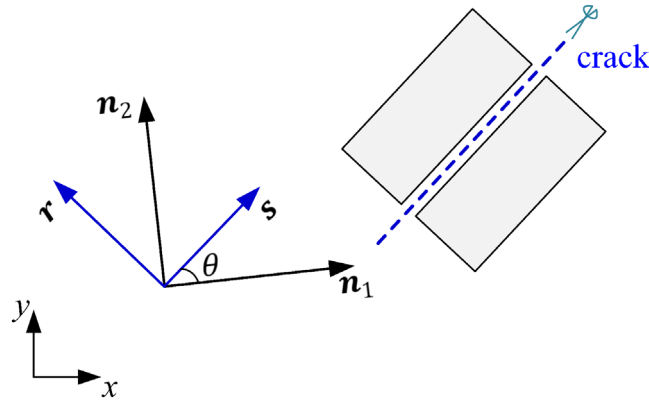
FIGURE 2 The relation between the local crack coordinate system, the principal strain, and the global coordinate system.

$\langle\cdot\rangle$ denotes the Macaulay brackets. λ and μ are the Lamé constants. $G_{\mathrm{I}c}$ and $G_{\mathrm{II}c}$ are respectively the mode-I and mode-II critical energy release rate.

2.2 | Directional split for crack-driving energy

To derive a kinematically consistent energy dissipation which considers the direction of the potential crack, the directional strain split is used in many papers for phase-field models. Let r denotes the crack normal vector and s the tangential vector which are parameterized by $s = (\cos\theta, \sin\theta)^{\mathrm{T}}$ and $r = (-\sin\theta, \cos\theta)^{\mathrm{T}}$, in which θ is the anticlockwise rotating angle between the major principal strain axis and the crack tangential vector, that is, n_1 and s, respectively (Figure 2).

The strain tensor $\varepsilon = \begin{bmatrix} \varepsilon_{rr} & \varepsilon_{rs} \\ \varepsilon_{sr} & \varepsilon_{ss} \end{bmatrix}$ in the local crack coordinate system is computed by

$$\begin{cases} \varepsilon_{rr} = \frac{\varepsilon_1 + \varepsilon_2}{2} + \frac{\varepsilon_1 - \varepsilon_2}{2}\cos(2\theta) \\ \varepsilon_{ss} = \frac{\varepsilon_1 + \varepsilon_2}{2} - \frac{\varepsilon_1 - \varepsilon_2}{2}\cos(2\theta) \\ \varepsilon_{rs} = \varepsilon_{sr} = \frac{\varepsilon_1 - \varepsilon_2}{2}\sin(2\theta) \end{cases} \tag{8}$$

ε_1 and ε_2 are, respectively, the major and minor principal strain.
To differentiate tensile/compressive/shear contribution from the strain components, ε is split by

$$\varepsilon = \varepsilon_{\mathrm{I}}^+ + \varepsilon_{\mathrm{II}}^+ + \varepsilon^- \tag{9}$$

$\varepsilon_{\mathrm{I}}^+$ is the tensile crack-driving part and is given by

$$\varepsilon_{\mathrm{I}}^+ = \begin{cases} \begin{pmatrix} \varepsilon_{rr} & 0 \\ 0 & \varepsilon_{ss} \end{pmatrix}, & \text{if } \varepsilon_{rr} + \frac{\lambda}{\lambda+2\mu}\varepsilon_{ss} > 0 \text{ and } \varepsilon_{ss} > 0 \\ \begin{pmatrix} \varepsilon_{rr} + \frac{\lambda}{\lambda+2\mu}\varepsilon_{ss} & 0 \\ 0 & 0 \end{pmatrix}, & \text{if } \varepsilon_{rr} + \frac{\lambda}{\lambda+2\mu}\varepsilon_{ss} > 0 \text{ and } \varepsilon_{ss} \le 0 \\ \begin{pmatrix} 0 & 0 \\ 0 & 0 \end{pmatrix}, & \text{if } \varepsilon_{rr} + \frac{\lambda}{\lambda+2\mu}\varepsilon_{ss} \le 0 \end{cases} \tag{10}$$

In Equation (10), $\varepsilon_{rr} + \frac{\lambda}{\lambda+2\mu}\varepsilon_{ss} > 0$ indicates a positive normal stress σ_{rr} on the potential crack surface because
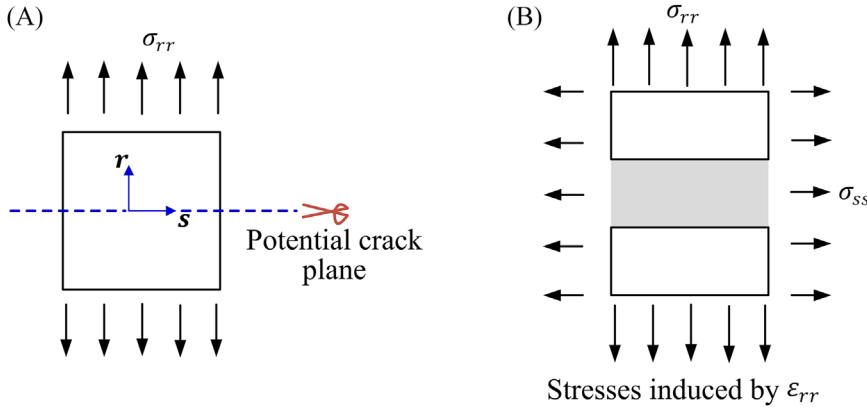
(A)

(B)

FIGURE 3 An arbitrary crack opening results in degraded stress in both directions.

$$\sigma_{rr} = \lambda(\varepsilon_{rr} + \varepsilon_{ss}) + 2\mu\,\varepsilon_{rr} = (\lambda + 2\mu)\left(\varepsilon_{rr} + \frac{\lambda}{\lambda + 2\mu}\varepsilon_{ss}\right) \tag{11}$$

This judging criterion assumes new fractures can sustain compressive, but not tensile normal stress perpendicular to its surface.[31]

In the second case of Equation (10), that is, $\varepsilon_{rr} + \frac{\lambda}{\lambda+2\mu}\varepsilon_{ss} > 0$ *and* $\varepsilon_{ss} \leq 0$, a degraded stress σ_I^+ is calculated as

$$\sigma_I^+ = \begin{pmatrix} \sigma_{rr} & 0 \\ 0 & \frac{\lambda}{(\lambda+2\mu)}\sigma_{rr} \end{pmatrix} \tag{12}$$

An arbitrary crack opening (given by ε_{rr}) results in a degraded stress in both normal and shear directions of the cracks. In this way, the lateral deformation or necking of the elastic material caused by Poisson's effect will be released completely in a fully damaged state[30,45] (depicted in Figure 3).

ε_{II}^+ is the shear crack-driving part and is given by

$$\varepsilon_{II}^+ = \begin{pmatrix} 0 & \varepsilon_{rs} \\ \varepsilon_{sr} & 0 \end{pmatrix} \tag{13}$$

ε^- is the remaining non-crack-driving part.

Then, the cracking direction is determined based on the F-criterion, that is, by searching the direction, which maximize $F(\theta)$ where

$$\theta = \arg\,max\,(F(\theta)) \tag{14}$$

$$F(\theta) = \frac{W_I^+(\theta)}{G_{Ic}} + \frac{W_{II}^+(\theta)}{G_{IIc}} = \frac{1}{2}\frac{\sigma_I^+ : \varepsilon}{G_{Ic}} + \frac{1}{2}\frac{\sigma_{II}^+ : \varepsilon}{G_{IIc}} \tag{15}$$

σ_I^+, σ_{II}^+, and σ^- are the counterparts for ε_I^+, ε_{II}^+, and ε^- and are given by

$$\sigma_I^+ = D : \varepsilon_I^+, \sigma_I I^+ = D : \varepsilon_I I^+, \sigma^- = D : \varepsilon^- \tag{16}$$

$\mathbb{D} = \lambda(\mathbf{I} \otimes \mathbf{I}) + 2\mu\mathbb{I}$ is the fourth-order elasticity tensor. I and $\mathbb{I}$ are, respectively, the second-order identity tensor and the fourth-order symmetric identity tensor.

To search the direction θ maximizing F, we combine Equations (10), (13), (15), and (16) to calculate the necessary condition $\frac{\partial F(\theta)}{\partial \theta} = 0$, and obtain
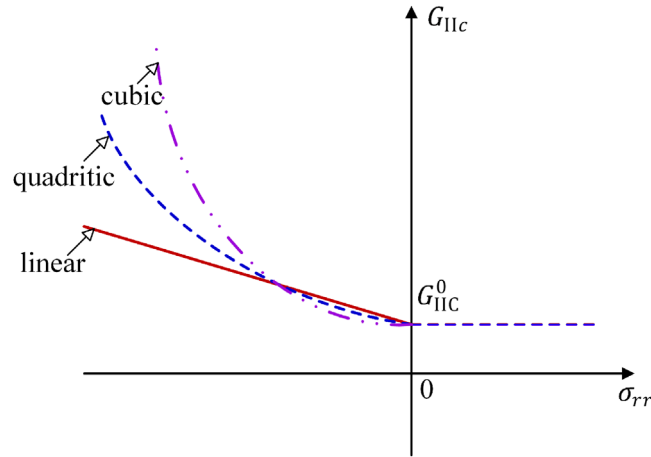
FIGURE 4 Linear/quadratic/cubic relationship between shear fracture energy and normal pressure.

(i) Case 1 ($\varepsilon_{rr} + \frac{\lambda}{\lambda+2\mu}\varepsilon_{ss} > 0$ and $\varepsilon_{ss} > 0$)

$$\frac{\partial F(\theta)}{\partial \theta} = \mu(\varepsilon_1 - \varepsilon_2)^2 \left(\frac{1}{G_{\mathrm{IIc}}} - \frac{1}{G_{\mathrm{Ic}}} \right) \sin(4\theta) \qquad (17)$$

(ii) Case 2 ($\varepsilon_{rr} + \frac{\lambda}{\lambda+2\mu}\varepsilon_{ss} > 0$ and $\varepsilon_{ss} \leq 0$)

$$\frac{\partial F(\theta)}{\partial \theta} = \frac{2\mu(\lambda+\mu)}{MG_{\mathrm{Ic}}} (\varepsilon_2^2 - \varepsilon_1^2) \sin(2\theta) + \mu(\varepsilon_1 - \varepsilon_2)^2 \left(\frac{1}{G_{\mathrm{IIc}}} - \frac{\mu}{MG_{\mathrm{Ic}}} \right) \sin(4\theta) \qquad (18)$$

(iii) Case 3 ($\varepsilon_{rr} + \frac{\lambda}{\lambda+2\mu}\varepsilon_{ss} \leq 0$)

$$\frac{\partial F(\theta)}{\partial \theta} = \mu(\varepsilon_1 - \varepsilon_2)^2 \frac{1}{G_{\mathrm{IIc}}} \sin(4\theta) \qquad (19)$$

where $M = \lambda + 2\mu$ is the one-dimensional constrained modulus.

For the above three cases, solving $\frac{\partial F(\theta)}{\partial \theta} = 0$ gives the following three possible solutions: $\theta = 0$, $\theta = \frac{1}{2}\cos^{-1}(\frac{(\lambda+\mu)G_{\mathrm{IIc}}}{MG_{\mathrm{Ic}}-\mu G_{\mathrm{IIc}}} \cdot \frac{\varepsilon_1+\varepsilon_2}{\varepsilon_1-\varepsilon_2})$, $\theta = \frac{\pi}{4}$. The three possible cracking angles are then used to compute $F(\theta)$, and the angle which gives the maximum $F(\theta)$ is chosen as the local potential crack direction. The calculated θ can be inherited by the voxel crack model[46,47] used in numerical manifold method (NMM) for the further contact simulation of the crack detached rock blocks, to complete the whole process from fracture initiation, propagation to the collapse of rock masses. More details will be introduced and investigated in our future work.

2.3 | Confinement-dependent G_{IIc} for directional split

To further consider the dependence of G_{IIc} on confinement, a non-constant G_{IIc} is used in this paper to calculate the cracking angle. Assume a linear relationship between the normal pressure σ_{rr} and G_{IIc} in the compressive regime, while constant in the tensile regime (Figure 4), that is,

$$G_{\mathrm{IIc}} = A\sigma_{rr-} + B, \quad (where) \; \sigma_{rr-} = \frac{\sigma_{rr} - abs(\sigma_{rr})}{2} \qquad (20)$$

A and B have the unit of [m] and [N $\cdot$ m^{-1}], respectively.

With this assumption, for case 3 $(\varepsilon_{rr} + \frac{\lambda}{\lambda+2\mu}\varepsilon_{ss} \leq 0)$, a different cracking angle should be computed to find the maximum $F(\theta)$. In this case,

$$W_{\mathrm{I}}^+ (\theta) = 0, \ W_{\mathrm{II}}^+ (\theta) = \frac{1}{2}\mu(\varepsilon_1 - \varepsilon_2)^2 \sin^2(2\theta), \ F(\theta) = \frac{W_{\mathrm{II}}^+(\theta)}{G_{\mathrm{II}c}} \tag{21}$$

Then, we have

$$\frac{\partial F(\theta)}{\partial\theta} = \frac{\mu(\varepsilon_1 - \varepsilon_2)^2 \sin(2\theta) \cdot \left(A\mu(\varepsilon_1 - \varepsilon_2)\cos^2(2\theta) + [2A(\lambda + \mu)(\varepsilon_1 + \varepsilon_2) + 2B]\cos(2\theta) + A\mu(\varepsilon_1 - \varepsilon_2)\right)}{(A[(\lambda + \mu)(\varepsilon_1 + \varepsilon_2) + \mu(\varepsilon_1 - \varepsilon_2)\cos(2\theta)] + B)^2} \tag{22}$$

If $A = 0$, which means a constant shear fracture energy over the entire stress state, we can have

$$2B \cos(2\theta) = 0 \Rightarrow \theta = \frac{\pi}{4} \tag{23}$$

If $A \neq 0$, we can have

$$\theta = \frac{1}{2}\cos^{-1}\left(\frac{-b + \sqrt{b^2 - 4a^2}}{2a}\right) \tag{24}$$

where

$$a = A\mu(\varepsilon_1 - \varepsilon_2), \ b = 2A(\lambda + \mu)(\varepsilon_1 + \varepsilon_2) + 2B \tag{25}$$

Similarly, if a quadratic relationship ($G_{\mathrm{II}c} = (A\langle\sigma_{nn}\rangle_- + B)^2$) is assumed, then the cracking angle θ is derived as

$$\theta = \frac{1}{2}\cos^{-1}\left(\frac{-A\mu(\varepsilon_1 - \varepsilon_2)}{A(\lambda + \mu)(\varepsilon_1 + \varepsilon_2) + B}\right) \tag{26}$$

If a cubic function ($G_{\mathrm{II}c} = (A\langle\sigma_{nn}\rangle_- + B)^3$) is assumed, then

$$\theta = \frac{1}{2}\cos^{-1}\left(\frac{-b + \sqrt{b^2 - 4ac}}{2a}\right) \tag{27}$$

where

$$a = -A\mu(\varepsilon_1 - \varepsilon_2), \ b = 2A(\lambda + \mu)(\varepsilon_1 + \varepsilon_2) + 2B, \ c = 3A\mu(\varepsilon_1 - \varepsilon_2) \tag{28}$$

This angle is added to the selection pool for calculating the cracking angle. An example of the calculation of θ in the principal strain plane is shown in Figure 5 for varying $G_{\mathrm{II}c}^0/G_{\mathrm{I}c}$ ratio. With decreasing $G_{\mathrm{II}c}^0$, the red region which stands for the crack propagation along the maximum shear direction ($\theta = 45^{\mathrm{o}}$) widens.

3 | NUMERICAL IMPLEMENTATION

The standard finite element discretization for the displacement field and phase field, and their variation and gradient read

$$u = \mathbf{N}_u \ \tilde{\mathbf{u}}, \ \delta u = \mathbf{N}_u \ \delta\tilde{\mathbf{u}}, \ \varepsilon = \mathbf{B}_u \ \tilde{\mathbf{u}} \tag{29}$$

$$d = \mathbf{N}_d \ \tilde{\mathbf{d}}, \ \delta d = \mathbf{N}_d \ \delta\tilde{\mathbf{d}}, \ \nabla d = \mathbf{B}_d \ \tilde{\mathbf{d}} \tag{30}$$
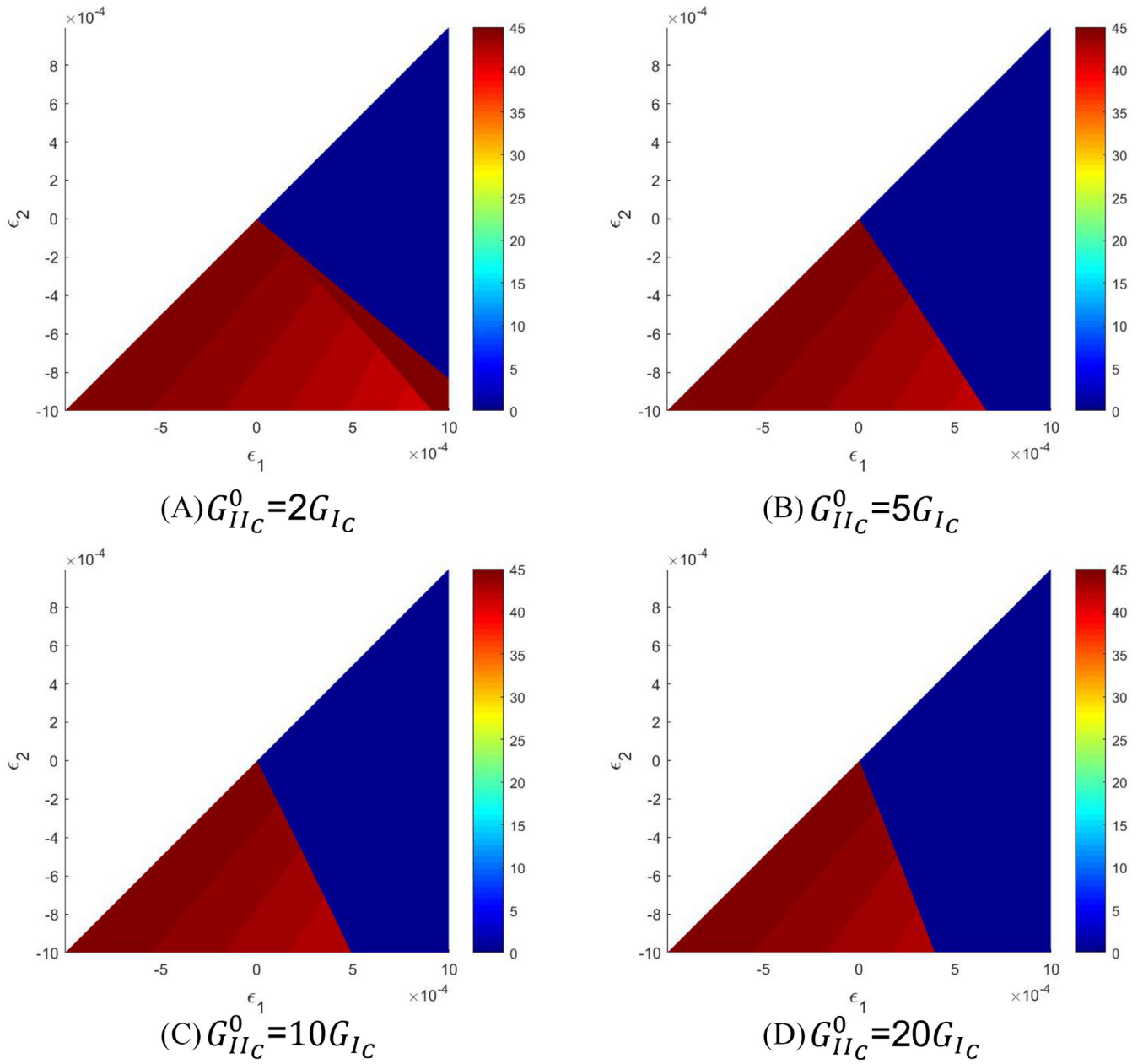
FIGURE 5   The calculation of θ in the principal strain plane (in degree).

N_u and N_d represent the shape functions for the displacement and phase field respectively. B_u and B_d are their derivatives where

$$
\mathbf{B}_u = \begin{bmatrix} \dfrac{\partial N_1^u}{\partial x} & 0 & \cdots & \dfrac{\partial N_i^u}{\partial x} & 0 \\[2mm] 0 & \dfrac{\partial N_1^u}{\partial y} & \cdots & 0 & \dfrac{\partial N_i^u}{\partial y} \\[2mm] \dfrac{\partial N_1^u}{\partial y} & \dfrac{\partial N_1^u}{\partial x} & \cdots & \dfrac{\partial N_i^u}{\partial y} & \dfrac{\partial N_i^u}{\partial x} \end{bmatrix}, \quad \mathbf{B}_d = \begin{bmatrix} \dfrac{\partial N_1^u}{\partial x} & \dfrac{\partial N_2^u}{\partial x} & \cdots & \dfrac{\partial N_i^u}{\partial x} \\[2mm] \dfrac{\partial N_1^u}{\partial y} & \dfrac{\partial N_2^u}{\partial y} & \cdots & \dfrac{\partial N_i^u}{\partial y} \end{bmatrix} \tag{31}
$$

$\tilde{\mathbf{u}}$ and $\tilde{\mathbf{d}}$ are nodal unknown vectors for the two fields.

A L G O R I T H M 1 Material cracking angle and $F(\theta)$ computation for the present phase-field model

---

Input: ε, $(\mathcal{H})^{t=t_{n-1}}$

Output: θ, $(\mathcal{H})^{t=t_n}$

  Calculate the valid angle for possible cracking directions
  under the current strain state:

  $\theta = 0, \theta = \frac{\pi}{4}, \theta = \frac{1}{2}\cos^{-1}(\frac{(\lambda+G)G_{\mathrm{IIc}}}{MG_{\mathrm{Ic}}-GG_{\mathrm{IIc}}} \cdot \frac{\varepsilon_1+\varepsilon_2}{\varepsilon_1-\varepsilon_2}), \theta =$
  $\frac{1}{2}\cos^{-1}(\frac{-b+\sqrt{b^2-4a^2}}{2a})$.
  Calculate the equivalent crack driving force $F(\theta)$ along these
  possible angles.

  Choose the angle θ which gives the maximum $F(\theta)$.

  Update the history variable $(\mathcal{H})^{t=t_n}$ according to Equation 38).

End

The weak form for Equations (5) and (6) can be written as

$$\int_{\Omega} \sigma : \nabla^{sym}\delta u \mathrm{d}\Omega = \int_{\Omega} f \cdot \delta u \mathrm{d}\Omega + \int_{\partial\Omega^t} t \cdot \delta u \mathrm{dS} \tag{32}$$

$$\int_{\Omega} \left(\frac{1}{l_0}d\delta d + l_0 \nabla d \nabla \delta d \right) \mathrm{d}\Omega = \int_{\Omega} 2(1-d)\mathcal{H}\delta d \mathrm{d}\Omega \tag{33}$$

Then, the discretized form is written as

$$(\delta\tilde{\mathbf{u}})^{\mathrm{T}} \int_{\Omega} (\mathbf{B}_u)^{\mathrm{T}}\frac{\partial\sigma}{\partial\varepsilon}\mathbf{B}_u \mathrm{d}\Omega\ \tilde{\mathbf{u}} = (\delta\tilde{\mathbf{u}})^{\mathrm{T}} \int_{\Omega} (\mathbf{N}_u)^{\mathrm{T}} \cdot f\mathrm{d}\Omega + (\delta\tilde{\mathbf{u}})^{\mathrm{T}} \int_{\partial\Omega^t} (\mathbf{N}_u)^{\mathrm{T}} \cdot t\mathrm{d}\Omega \tag{34}$$

$$\left(\delta\tilde{\mathbf{d}}\right)^{\mathrm{T}} \int_{\Omega} \left\{ \frac{1}{l_0}(\mathbf{N}_d)^{\mathrm{T}}\mathbf{N}_d + l_0(\mathbf{B}_d)^{\mathrm{T}}\mathbf{B}_d \right\}\mathrm{d}\Omega\tilde{\mathbf{d}} + \left(\delta\tilde{\mathbf{d}}\right)^{\mathrm{T}} \int_{\Omega} 2\mathcal{H}(\mathbf{N}_d)^{\mathrm{T}}\mathbf{N}_d\mathrm{d}\Omega\ \tilde{\mathbf{d}} = \left(\delta\tilde{\mathbf{d}}\right)^{\mathrm{T}} \int_{\Omega} 2\mathcal{H}(\mathbf{N}_d)^{\mathrm{T}}\mathrm{d}\Omega \tag{35}$$

For arbitrary admissible $\delta\tilde{\mathbf{u}}$ and $\delta\tilde{\mathbf{d}}$, Equations (34) and (35) hold. Then, we have

$$\int_{\Omega} (\mathbf{B}_u)^{\mathrm{T}}\frac{\partial\sigma}{\partial\varepsilon}\mathbf{B}_u \mathrm{d}\Omega\ \tilde{\mathbf{u}} = \int_{\Omega} (\mathbf{N}_u)^{\mathrm{T}} \cdot f\mathrm{d}\Omega + \int_{\partial\Omega^t} (\mathbf{N}_u)^{\mathrm{T}} \cdot t\mathrm{d}\Omega \tag{36}$$

$$\int_{\Omega} \left\{ \frac{1}{l_0}(\mathbf{N}_d)^{\mathrm{T}}\mathbf{N}_d + l_0(\mathbf{B}_d)^{\mathrm{T}}\mathbf{B}_d + 2(\mathbf{N}_d)^{\mathrm{T}}\mathcal{H}\mathbf{N}_d \right\}\mathrm{d}\Omega\ \tilde{\mathbf{d}} = \int_{\Omega} 2(\mathbf{N}_d)^{\mathrm{T}}\mathcal{H}\mathrm{d}\Omega \tag{37}$$

To enforce crack irreversibility, a history variable $\mathcal{H}$ is used in Equations (35) and (37), which is defined as

$$(\mathcal{H})^{t=t_n} = max\left\{ (\mathcal{H})^{t=t_{n-1}}, F(\theta) \right\} \tag{38}$$

$F(\theta)$ is calculated in each iteration in each loading step for every quadrature points. The pseudo code for the cracking angle (therefore the crack surface normal) and $F(\theta)$ computation based on the current strain state is presented as Algorithm 1:

The displacement balance subproblem (Equation (36)) is nonlinear due to the direction-based strain energy decomposition, as with many decomposition schemes accounting for tension/compression asymmetry. In the commonly adopted staggered algorithm for solving phase field models, Equations (36) and (37) are alternatively solved in every loading step until convergence is achieved based on the selected criterion. However, when solving the displacement field u with a fixed phase field d, the tangent stiffness term $\frac{\partial\sigma}{\partial\varepsilon}$ in Equation (36) depends on the cracking angle (and therefore u) which results

FIGURE 6 Short core in compression tests: (A) experimental configuration; (B) numerical configuration.
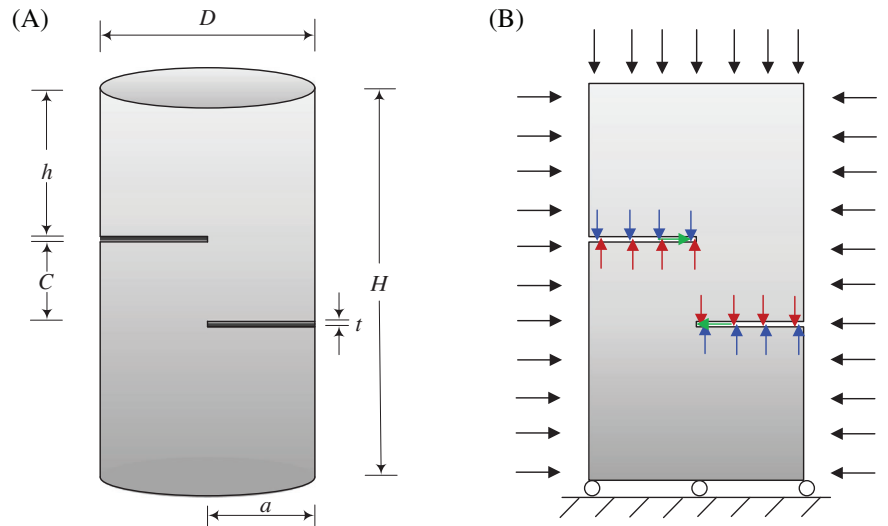
in nonlinearity, because only σ_{I}^+ and σ_{II}^+ are degraded

$$\frac{\partial \sigma}{\partial \varepsilon} = (1-d)^2 \left(\frac{\partial \sigma_{\mathrm{I}}^+}{\partial \varepsilon} + \frac{\partial \sigma_{\mathrm{II}}^+}{\partial \varepsilon} \right) + \frac{\partial \sigma^-}{\partial \varepsilon} \tag{39}$$

In this paper, the hybrid formulation proposed by Ambati et al.[48] is used to avoid the iterations required in solving Equation (36), which simplifies Equation (39) to

$$\frac{\partial \sigma}{\partial \varepsilon} = (1-d)^2 \mathbf{D}_e \tag{40}$$

$\mathbf{D}_e$ is the elasticity matrix for the undamaged material. The convergence is judged by residuals and nodal updates for both fields in this paper. The alternate minimization or the so-called staggered algorithm has been proven to be more robust than the monolithic algorithm in solving phase-field equations. Noteworthy are date-driven models[49–51] recently developed for solving phase-field problems monolithically.

4 | NUMERICAL EXAMPLES

In this paper, all existing cracks or notches are represented as meshed-in and pre-existing flaws, and their surface contact is not considered. Plane stress state is assumed for all the examples.

4.1 | Short core in compression (SCC) tests

To investigate the applicability of the proposed model in capturing the confinement effect, the short core in compression tests, which are widely used for examining rock shear fracture behaviors,[52–54] are first modeled. The geometrical and material parameters are taken from.[54] As shown in Figure 6, the granite core diameter $D = 50$ mm and the core height $H = 100$ mm. The prefabricated notches with an aperture of $t = 1$ mm extend from the outer surface to the core center with a net distance $C = 39$ mm. The material parameters of the granite are listed in Table 1.

According to,[54] all the surfaces of SCC specimens are subjected to the same confining pressure under triaxial loading. The mode-II fracture toughness are then calculated based on the ultimate bearing capacity under different confining pressure, and the morphology features of shear fracture surfaces are studied from three-dimensional optical scanner data. Due to the detailed experimental data regarding mode-II rock fracture in,[54] the SCC experiments are chosen here to verify the proposed model. Using the relation between $K_{\mathrm{Ic}}(K_{\mathrm{IIc}})$ and $G_{\mathrm{Ic}}(G_{\mathrm{IIc}})$ from linear elastic fracture mechanics, we have $G_{\mathrm{Ic}} = 0.091\mathrm{N/mm}$ and $G_{\mathrm{IIc}} = (0.024P + 0.561)^2$ N/mm which equates to $A = -0.024\sqrt{\mathrm{N/mm}}/\mathrm{MPa}$, $B = 0.561\sqrt{\mathrm{N/mm}}$ in Equation (24). A two-dimensional plane numerical model instead of a three-dimensional setup is established as shown in Figure 6B for computational efficiency. The uniform confining pressure are applied as a uniform isotropic initial

TABLE 1 The mechanical parameters of granite[54].

Properties	Value
Young's modulus E (GPa)	40.16
Poisson's ratio ν	0.31
Brazilian tensile strength σ_t (MPa)	11.3
Cohesion c (MPa)	28.81
Internal friction angle (°)	56
Mode-I fracture toughness K_{Ic} (MPa $\cdot \sqrt{\text{m}}$)	1.91
Mode-II fracture toughness K_{IIc} (MPa $\cdot \sqrt{\text{m}}$)	3.77+0.152P[a]

[a]P is the confining pressure.
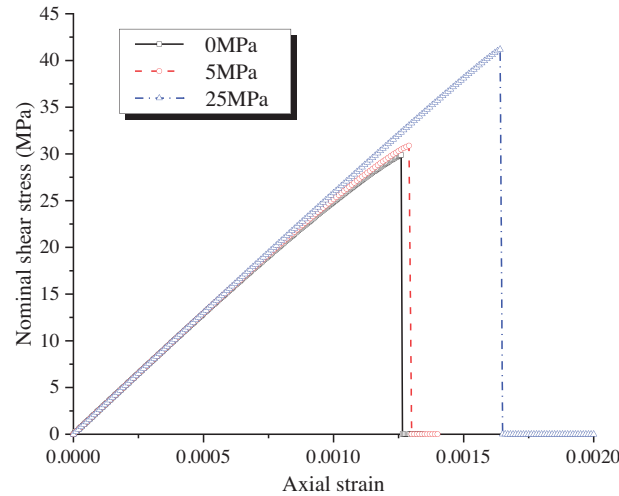
FIGURE 7 Nominal shear stress-axial strain curves under different confining pressure.

compressive strain. The bottom boundary is fixed in the vertical direction and a pin is applied to the middle of the top boundary. The top boundary is then compressed by a downward displacement with an increment of $\Delta u = 0.001$ mm. The phase-field length parameter is set as $l_0 = 0.4$ mm. Quadrilateral linear elements (141,255) are used to discretize the whole analysis domain with the central area locally refined. The characteristic mesh size in the central region is $h = 0.12$ mm.

The SCC tests under 0 MPa/5 MPa/25 MPa confining pressure are modeled using the proposed numerical model. The obtained nominal shear stress-axial strain curves are shown in Figure 7. An approximately linear stress-strain response is observed until an abrupt brittle failure occurs. The nominal peak shear stress shows an increasing trend with elevated confining pressure, which is consistent with experimental findings. However, due to the ignorance of initial porosity and micro-cracks of the present model, discrepancy exists in the pre-peak region when compared to the experimental data in.[54]

The failure surfaces obtained by experiments and numerical models under different confining pressure are then compared. As can be seen from Figure 8, the ultimate failure plane forms between the upper and lower notches, showing an upright shear fracture behavior. In addition, with elevated confining pressure, the failure plane becomes smoother, which is consistent with experimental results. In,[54] the fracture roughness is quantified by the fractal dimension D, and D shows a degrading trend with confining pressure. In the numerical model, the fractal dimension cannot be easily measured, but the tortuosity of the ultimate failure plane shows a distinctly similar trend.

To investigate the influence of discretization and the phase-field length parameter on material behaviors, additional simulations have been performed. At first different discretization with characteristic mesh size $h = 0.2, 0.16, 0.12, 0.08, 0.05$ mm in the refined zone and a fixed phase-field length parameter $l_0 = 0.4$ mm for the cases under 0 and 25 MPa confinement is utilized. The obtained failure patterns are shown in Figure 9 and Figure 10. As shown, convergence with refined discretization is observed. Then the phase-field length parameter l_0 is varied with the same mesh $h = 0.12$ mm for the same confinement scenarios. The obtained nominal shear stress versus l_0 is plotted in Figure 11, and the failure surfaces are compared in Figures 12 and 13. For both loading cases, with decreasing length parameter l_0, the failure strength increases and the crack sharpens.

(A)   (B)   (C)
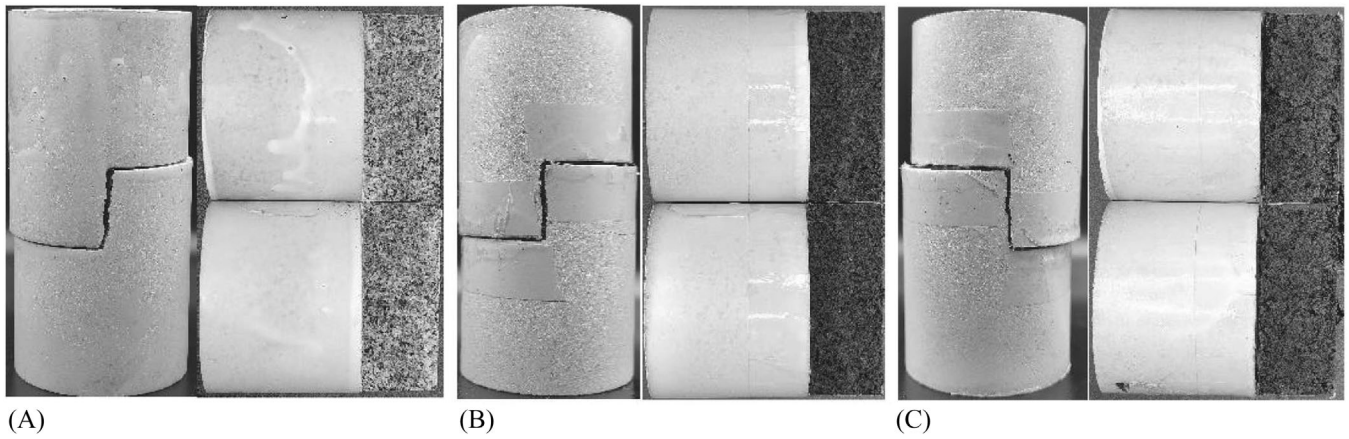
FIGURE 8   Failure surfaces obtained by numerical models (left column) and experiments (right column) under different confining pressure: (A) $P = 0$ MPa; (B) $P = 5$ MPa; (C) $P = 25$ MPa.

(A) $h = 0.16$mm   (B) $h = 0.12$mm   (C) $h = 0.08$mm
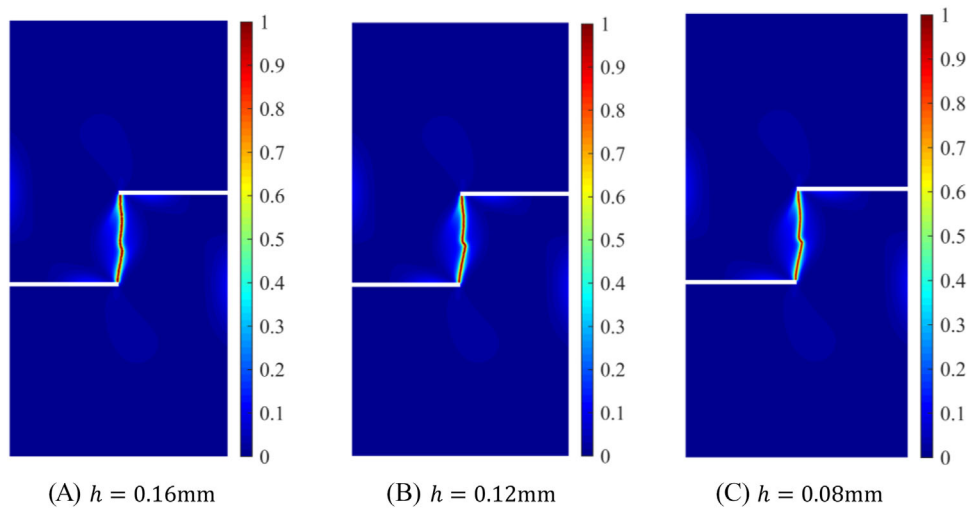
FIGURE 9   Failure surfaces with different discretization under no confining pressure.

(A) $h = 0.2$mm   (B) $h = 0.12$mm   (C) $h = 0.05$mm
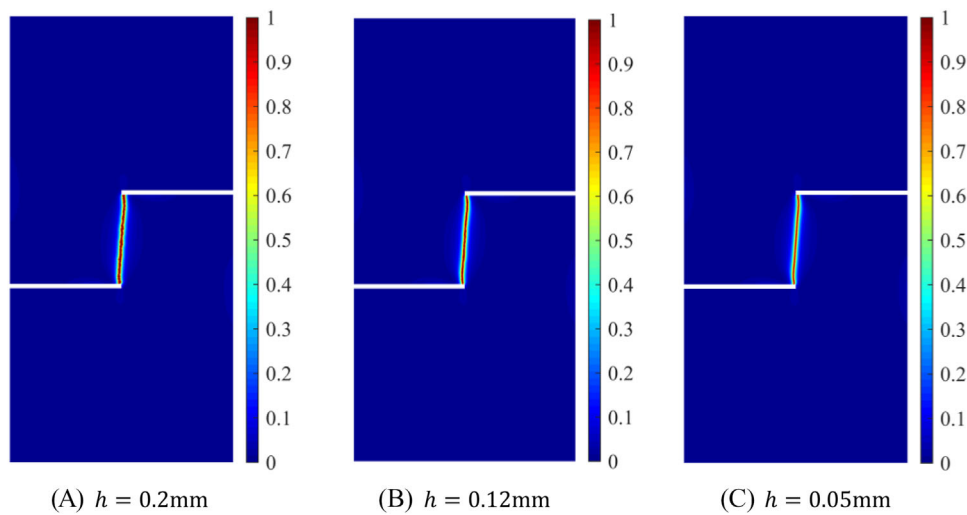
FIGURE 10   Failure surfaces with different discretization under confining pressure $P = 25$ MPa.
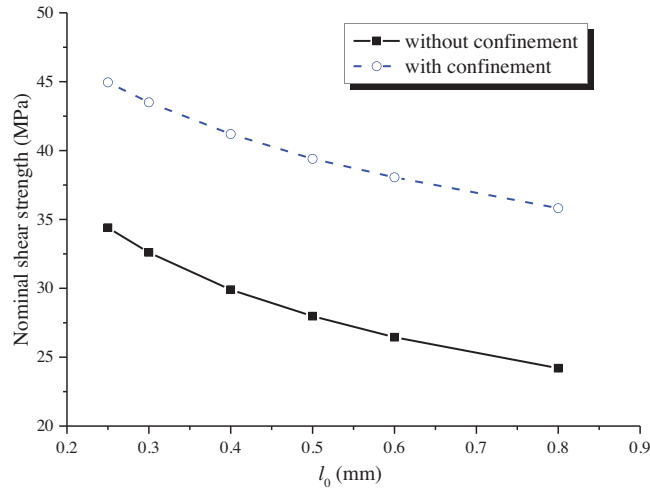
FIGURE 11 Nominal shear strength with different phase-field length parameters.

(A)$l_0 = 0.4mm$ (B)$l_0 = 0.3mm$ (C)$l_0 = 0.25mm$
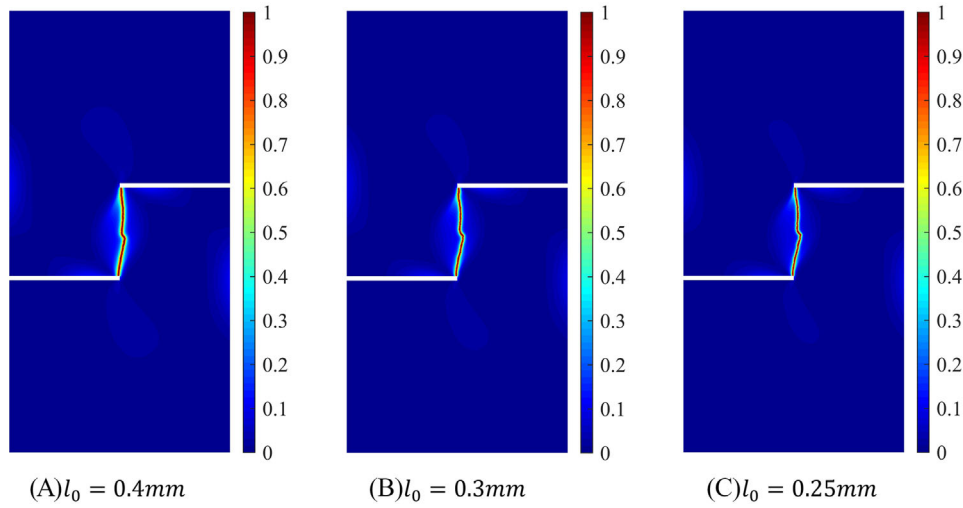
FIGURE 12 Failure surfaces with different phase field length parameter under no confining pressure.

(A)$l_0 = 0.8mm$ (B)$l_0 = 0.6mm$ (C)$l_0 = 0.5mm$
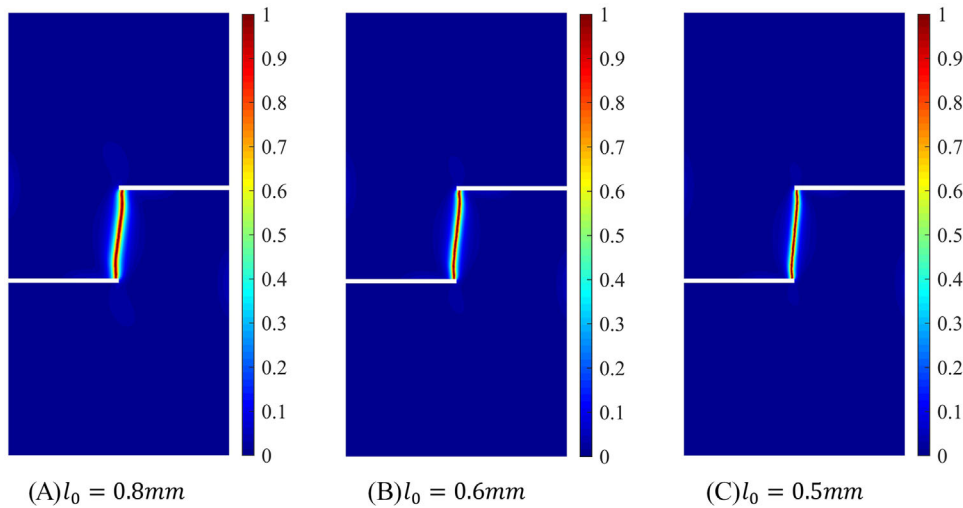
FIGURE 13 Failure surfaces with different phase field length parameter under confining pressure $P = 25$ MPa.
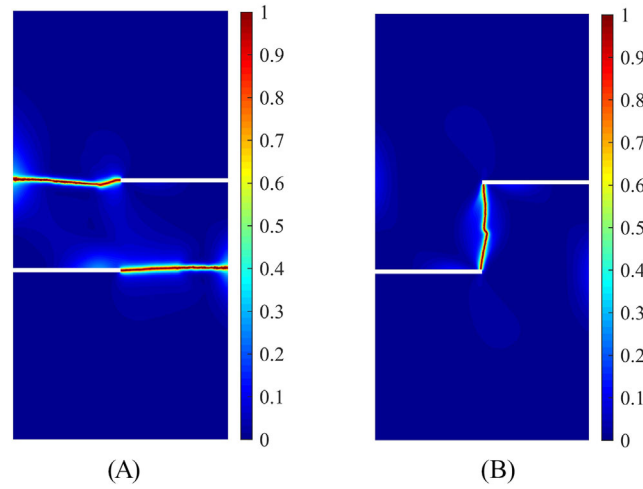
FIGURE 14 The failure surfaces obtained: (A) without confinement effect; (B) with confinement effect.
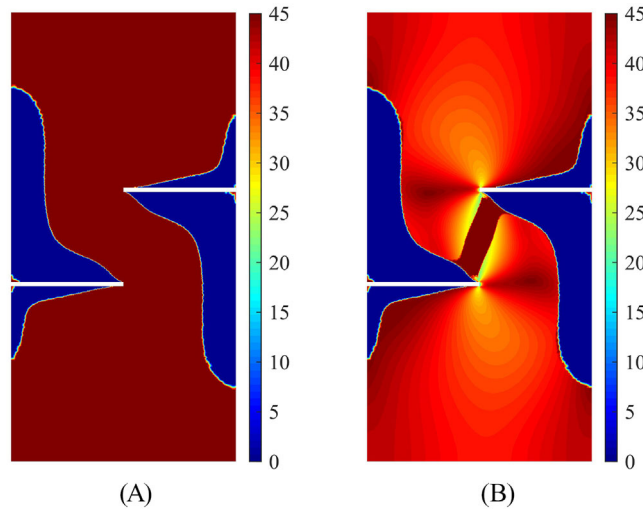
FIGURE 15 The cracking angle θ obtained (in degree) when $u_y^* = 0.079$ mm: (A) without confinement effect; (B) with confinement effect.

To further demonstrate the necessity of incorporating the confining pressure dependent mode-II fracture energy, we deactivate the fourth solution (Equation 26) for the cracking angle calculation and rerun the simulation with $l_0 = 0.4$ mm and mesh size $h = 0.12$ m. The obtained cracking pattern is plotted in Figure 14A). As seen, the model without incorporating confinement effect produces erroneous horizontal cracks.

We plot also the cracking angle θ and F-contours of the above two models obtained in one pre-peak loading step (with a downward displacement $u_y^* = 0.079$ mm) in Figures 15 and 16. Differences in the cracking angle distribution can be observed, especially around the notch front. For the model without confinement effect, the normalized crack driving force F concentrates right ahead of the notch front, whereas for the proposed approach with confinement effect, F concentrates in the central area between two notches.

To quantitatively demonstrate the difference between the two models, the strain tensor of the material point lying 1 mm horizontally ahead of the upper notch tip is analyzed. For the model without confinement effect, the strain tensor $\varepsilon = \begin{bmatrix} -5.317 \times 10^{-4} & -1.3685 \times 10^{-4} \\ -1.3685 \times 10^{-4} & -2.586 \times 10^{-3} \end{bmatrix}$. The calculated cracking angle $\theta = 45°$ and the equivalent cracking driving force $F = 0.093$/mm. While for the model with confinement effect, the strain tensor $\varepsilon = \begin{bmatrix} -5.417 \times 10^{-4} & -1.347 \times 10^{-4} \\ -1.347 \times 10^{-4} & -1.962 \times 10^{-3} \end{bmatrix}$. The calculated cracking angle $\theta = 38.4°$ and the equivalent cracking driving force

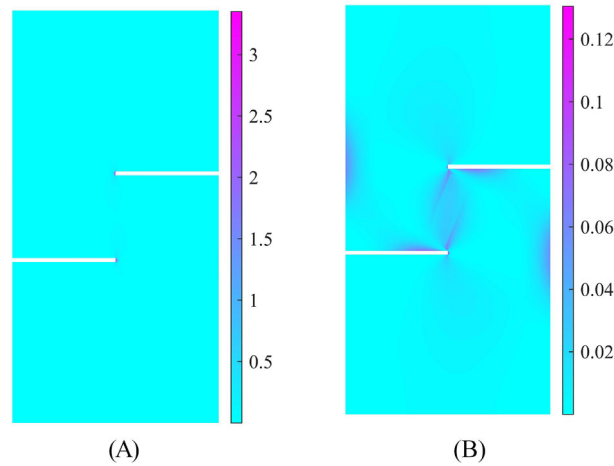**FIGURE 16** The F obtained when $u_y^* = 0.079$ mm: (A) without confinement effect; (B) with confinement effect.
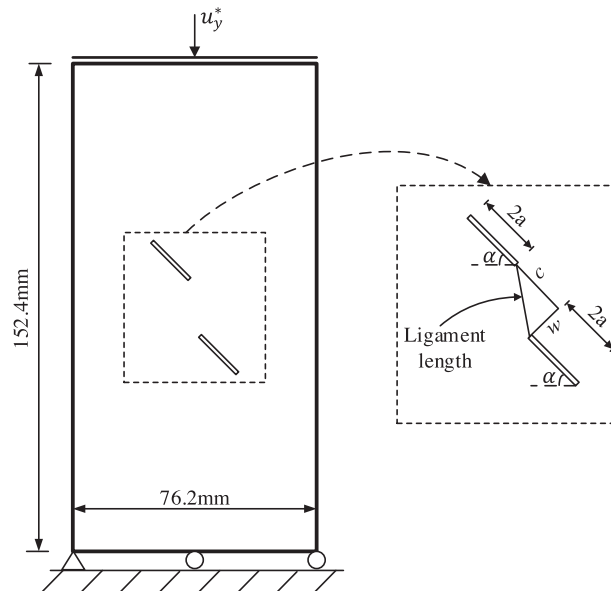

FIGURE 17 Rock-like specimen with two inclined flaws.

$F = 0.0031$/mm. Obviously, when the confinement effect is not incorporated, the predicted cracking is along the maximum shear direction under compressive-shear loading. With the proposed model, the maximum shear direction corresponds to a larger normal stress $\sigma_{rr} = -72.86$ MPa and gives $G_{IIc} = 5.493$N/mm. While along $\theta = 38.4^o$ plane, although with a smaller shear stress, the smaller $\sigma_{rr} = -67.83$ MPa gives a smaller $G_{IIc} = 4.942$N/mm and therefor a larger F.

4.2 | Rock-like specimen with coplanar and noncoplanar flaws

Mixed-mode fracture in rock-like specimens containing two flaws shown in Figure 17 studied by Bobet and Einstein[55–57] is then tested. The specimen is 76.2 mm ×152.4 mm (width × height), and the length and width of the initial flaws are $2a = 12.7$ mm and 0.1 mm. The configuration of the two flaws is described by "$\alpha - c - w$" where α denotes inclination angle, c denotes continuity, and w denotes spacing. We simulate two noncoplanar cases "$45^o - a - 2a$" and "$45^o - 2a - 2a$" and one coplanar case "$60^o - 0 - 2a$." The elasticity parameters are measured in[55,56] and directly adopted in the simulation: $E = 5.96$ GPa, $\nu = 0.24$. In the previous simulation,[43] the phase-field length parameter l_0 is set as 0.2 mm.
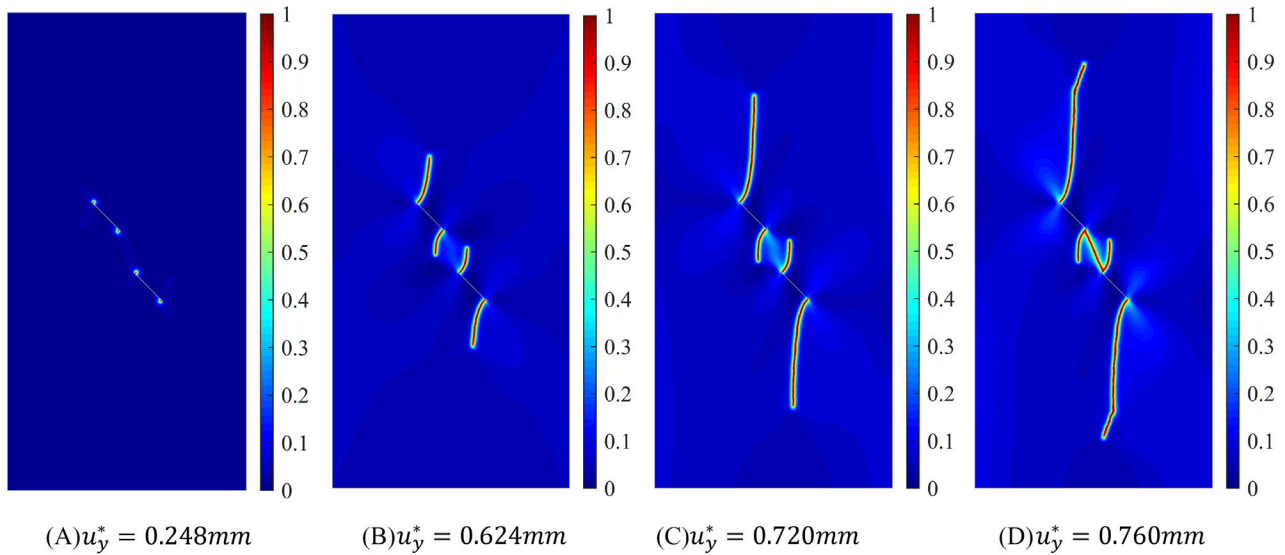
(A) $u_y^* = 0.248mm$ (B) $u_y^* = 0.624mm$ (C) $u_y^* = 0.720mm$ (D) $u_y^* = 0.760mm$

FIGURE 18 Crack propagation process for the noncoplanar configuration "$45^o - a - 2a$."

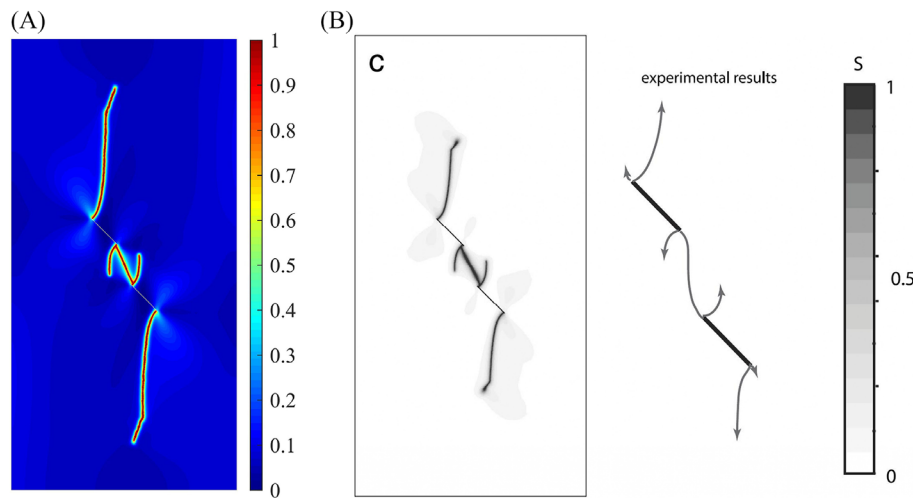**FIGURE 19** Crack patterns for rock-like specimens for the "$45^o - a - 2a$" configuration: (A) the present simulation; (B) simulation results by Zhang et al.[20] and the experiment.

The tensile and shear fracture energies are then calibrated to match the experimental coalescence stresses and are given by $G_{Ic} = 0.016$N/mm and $G_{IIc} = 0.205$N/mm. In this paper, the phase-field length parameter l_0 is set as 0.5 mm and mode-I fracture energy G_{Ic} is set as 0.04N/mm to keep $\frac{G_{Ic}}{l_0}$ unchanged. The mode-II fracture energy is then calibrated to match the coalescence stresses, and is given by $G_{IIc}^0 = 0.41$N/mm and $G_{IIc}^0(\sigma_{rr} = 30$ MPa$) = 2G_{IIc}^0$.

The noncoplanar case "$45^o - a - 2a$" is first presented. The region where the crack is likely to propagate is refined a priori with a mesh size $h = 0.25$ mm. In total the mesh includes 172156 quadrilateral elements. The simulated crack propagation process is shown in Figure 18. At first wing cracks initiate from both tips of both flaws (Figure 16A), then wing cracks continue to propagate but with an uneven speed (Figure 18B and 18C). Finally, an oblique crack connects the inner two tips, as shown in Figure 18D. Figure 19 shows the consistency of the present simulation with the results by Zhang et al.[20] and the experiment.

Then, the noncoplanar configuration "$45^o - 2a - 2a$" is studied. In total the mesh includes 172,365 quadrilateral elements. The crack propagation process and final crack pattern are presented in Figure 20. Similar to the previous case, the tensile wing cracks initiate and propagate before the coplanar shear cracks, but the coalescence pattern is not the same.
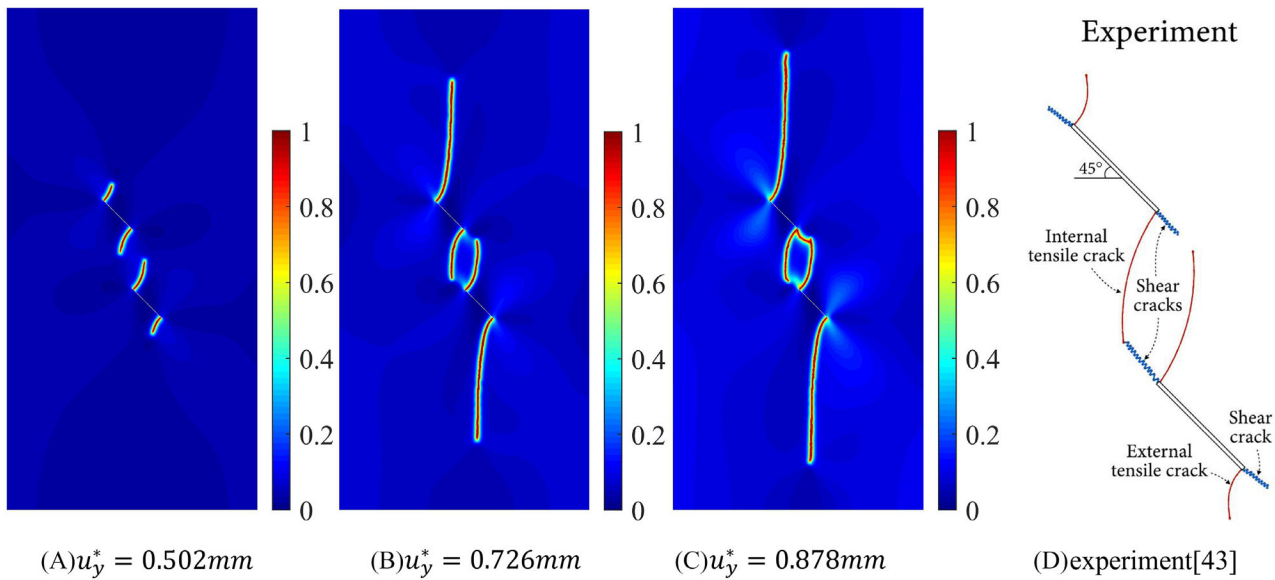
FIGURE 20 Crack propagation process and final crack patterns for the "$45^\circ - 2a - 2a$" configuration: simulation and experimental results.
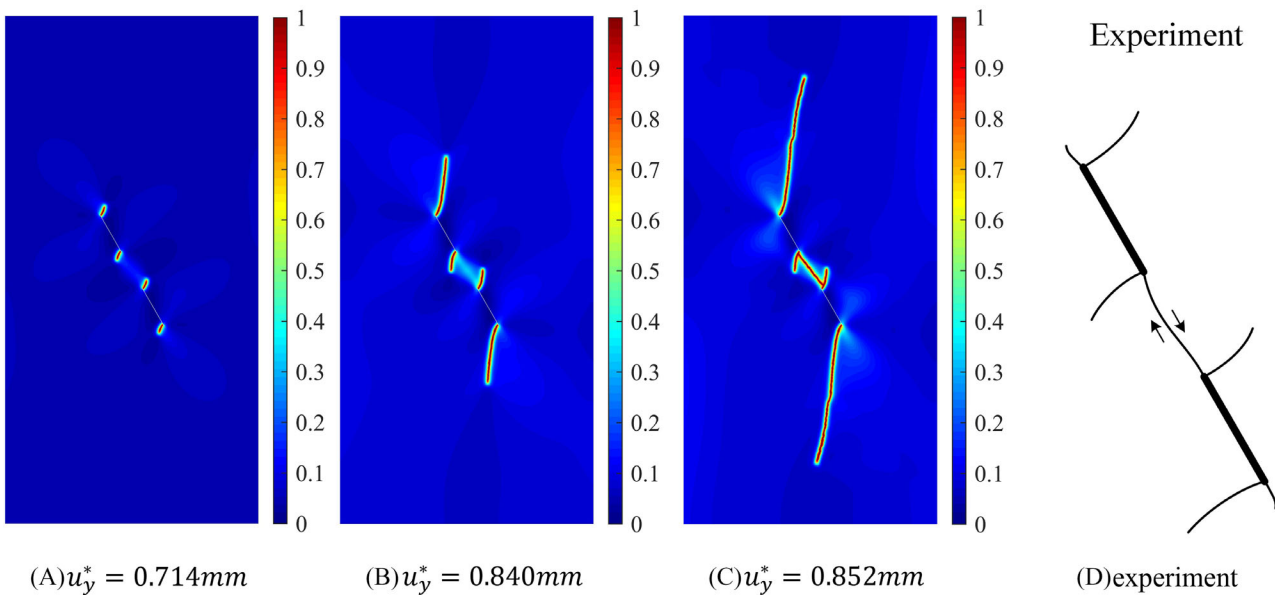

FIGURE 21 Crack propagation process and final crack patterns for the "$60^\circ - 0 - 2a$" configuration: simulation and experimental results. The experimental is redrawn from.[57]

In this case, the coalescence is generated by a coplanar shear crack from one tip joining the tensile wing crack from the other tip, which is also consistent with experimental findings.[43]

For the coplanar configuration "$60^\circ - 0 - 2a$," the analysis domain is discretized by 138,656 quadrilateral elements. Figure 21 presents the final crack pattern as compared to the experimental results in.[57] The coalescence type is characterized by secondary shear crack between the inner two crack tips, consistent with the statement in.[57]

For a quantitative comparison, the coalescence stress level for the above three cases is presented in Figure 22 together with experimental results. The maximum relative error is around 9.59% ,which shows good consistency. So far, the potential of the proposed model in capturing crack pattern and failure strength has been validated.
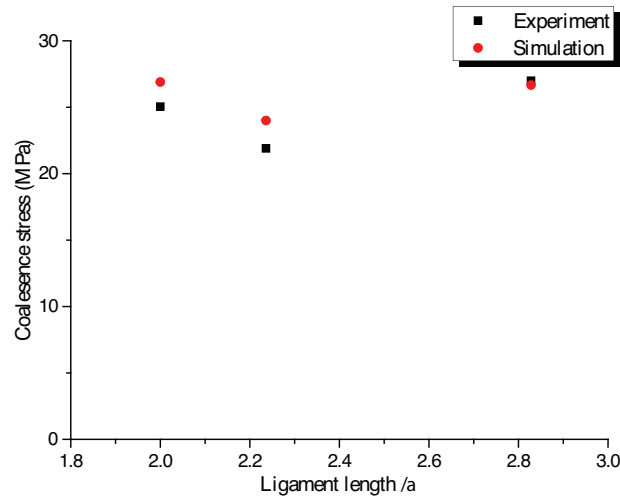
FIGURE 22 Crack coalescence stress for rock-like specimen with coplanar and non-coplanar flaws.

5 | CONCLUSION

In this paper, a phase-field formulation based on an extended F-criterion is proposed to simulate tensile-compressive-shear rock fractures. The phase-field crack-driving energy decomposition is determined by a direction search which maximizes the local fracture dissipation based on the F-criterion. In compressive-shear states, the computation is supplemented by an explicitly expressed confinement-dependent mode-II fracture energy. The cracking angle is obtained relying on both the fracture energy and strain states, which is a critical parameter for the future contact simulation of the crack detached rock blocks. This extension provides the present formulation with the ability to capture the pressure-sensitivity of rock and rock-like materials. Fracture from notches and coplanar/noncoplanar cracks in rock and rock-like specimens demonstrates the ability of the present model in capturing tensile-compressive-shear rock fracture behaviors.

Simple generic relationships between the normal stress and mode-II fracture energy are assumed to derive the analytical solution of the cracking direction, which can be generalized for more complex occasions. The adopted formulation is variationally inconsistent because of the incorporation of the history variable accounting for crack irreversibility and a hybrid strategy in calculating damaged stress for the simplified displacement subproblem. The influence of a hybrid formulation on crack evolution should be further explored. Extension to 3D should also be sought after proper consideration of the intermediate stress. Drastic changes of cracking directions are one of the main limitations of this paper, as with many directional-split based phase-field models. Studies on dealing with multiple cracking directions will be carried out in the future.

DATA AVAILABILITY STATEMENT
Data from the numerical analyses discussed in this paper can be made available to interested readers upon direct request to the authors.

ORCID
Jie Wu https://orcid.org/0000-0002-4107-8336

REFERENCES
1. Francfort GA, Marigo J. Revisiting brittle fracture as an energy minimization problem. *J Mech Phys Solids*. 1998;46:1319-1342.
2. Bourdin B, Francfort GA, Marigo J-J. Numerical experiments in revisited brittle fracture. *J Mech Phys Solids*. 2000;48:797-826. doi:10.1016/S0022-5096(99)00028-9

3. Tanné E, Li T, Bourdin B, Marigo JJ, Maurini C. Crack nucleation in variational phase-field models of brittle fracture. *J Mech Phys Solids*. 2018;110:80-99. doi:10.1016/j.jmps.2017.09.006

4. Wu JY. A unified phase-field theory for the mechanics of damage and quasi-brittle failure. *J Mech Phys Solids*. 2017;103:72-99. doi:10.1016/j.jmps.2017.03.015

5. Geelen RJM, Liu Y, Hu T, Tupek MR, Dolbow JE. A phase-field formulation for dynamic cohesive fracture. *Comput Methods Appl Mech Eng*. 2019;348:680-711. doi:10.1016/j.cma.2019.01.026

6. Chen L, de Borst R. Phase-field modelling of cohesive fracture. *Eur J Mech A Solids*. 2021;90. doi:10.1016/j.euromechsol.2021.104343

7. Borden MJ, Verhoosel C, Scott MA, Hughes TJR, Landis CM. A phase-field description of dynamic brittle fracture. *Comput Methods Appl Mech Eng*. 2012;217-220:77-95. doi:10.1016/j.cma.2012.01.008

8. Hofacker M, Miehe C. A phase field model of dynamic fracture: robust field updates for the analysis of complex crack patterns. *Int J Numer Methods Eng*. 2013;93:276-301. doi:10.1002/nme.4387

9. Ren HL, Zhuang XY, Anitescu C, Rabczuk T. An explicit phase field method for brittle dynamic fracture. *Comput Struct*. 2019;217:45-56. doi:10.1016/j.compstruc.2019.03.005

10. Ambati M, Gerasimov T, de Lorenzis L. Phase-field modeling of ductile fracture. *Comput Mech*. 2015;55:1017-1040. doi:10.1007/s00466-015-1151-4

11. Borden MJ, Hughes TJR, Landis CM, Anvari A, Lee IJ. A phase-field formulation for fracture in ductile materials: finite deformation balance law derivation, plastic degradation, and stress triaxiality effects. *Comput Methods Appl Mech Eng*. 2016;312:130-166. doi:10.1016/j.cma.2016.09.005

12. You T, Waisman H, Zhu QZ. Brittle-ductile failure transition in geomaterials modeled by a modified phase-field method with a varying damage-driving energy coefficient. *Int J Plast*. 2021;136:102836. doi:10.1016/j.ijplas.2020.102836

13. You T, Waisman H, Chen WZ, Shao JF, Zhu QZ. A novel micromechanics-enhanced phase-field model for frictional damage and fracture of quasi-brittle geomaterials. *Comput Methods Appl Mech Eng*. 2021;385:114060. doi:10.1016/j.cma.2021.114060

14. Miehe C, Schänzel LM, Ulmer H. Phase field modeling of fracture in multi-physics problems. Part I. Balance of crack surface and failure criteria for brittle crack propagation in thermo-elastic solids. *Comput Methods Appl Mech Eng*. 2015;294:449-485. doi:10.1016/j.cma.2014.11.016

15. Asur Vijaya Kumar PK, Dean A, Reinoso J, Paggi M. Nonlinear thermo-elastic phase-field fracture of thin-walled structures relying on solid shell concepts. *Comput Methods Appl Mech Eng*. 2022;396:115096. doi:10.1016/j.cma.2022.115096

16. Miehe C, Mauthe S. Phase field modeling of fracture in multi-physics problems. Part III. Crack driving forces in hydro-poro-elasticity and hydraulic fracturing of fluid-saturated porous media. *Comput Methods Appl Mech Eng*. 2016;304:619-655. doi:10.1016/j.cma.2015.09.021

17. Zhou S, Zhuang X, Rabczuk T. Phase field method for quasi-static hydro-fracture in porous media under stress boundary condition considering the effect of initial stress field. *Theor Appl Fract Mech*. 2020;107. doi:10.1016/j.tafmec.2020.102523

18. Amor H, Marigo JJ, Maurini C. Regularized formulation of the variational brittle fracture with unilateral contact: numerical experiments. *J Mech Phys Solids*. 2009;57:1209-1229. doi:10.1016/j.jmps.2009.04.011

19. Miehe C, Welschinger F, Hofacker M. Thermodynamically consistent phase-field models of fracture: variational principles and multi-field FE implementations. *Int J Numer Methods Eng*. 2010;83:1273-1311. doi:10.1002/nme.2861

20. Zhang X, Sloan SW, Vignes C, Sheng D. A modification of the phase-field model for mixed mode crack propagation in rock-like materials. *Comput Methods Appl Mech Eng*. 2017;322:123-136. doi:10.1016/j.cma.2017.04.028

21. Shen B, Stephansson O. Modification of the G-criterion for crack propagation subjected to compression. *Eng Fract Mech*. 1994;47:177-189. doi:10.1016/0013-7944(94)90219-4

22. Liu S, Wang Y, Peng C, Wu W. A thermodynamically consistent phase field model for mixed-mode fracture in rock-like materials. *Comput Methods Appl Mech Eng*. 2022;392:114642. doi:10.1016/j.cma.2022.114642

23. Zhou S, Zhuang X, Rabczuk T. Phase field modeling of brittle compressive-shear fractures in rock-like materials: a new driving force and a hybrid formulation. *Comput Methods Appl Mech Eng*. 2019;355:729-752. doi:10.1016/j.cma.2019.06.021

24. Xu Y, Zhou S, Xia C, Hu Y. A new phase field model for mixed-mode brittle fractures in rocks modified from triple shear energy criterion. *Acta Geotech*. 2022;17:5613-5637. doi:10.1007/s11440-022-01589-3

25. Jia ZM, Zhou XP, Berto F. Compressive-shear fracture model of the phase-field method coupled with a modified Hoek–Brown criterion. *Int J Fract*. 2021;229:161-184. doi:10.1007/s10704-021-00546-7

26. Strobl M, Seelig T. A novel treatment of crack boundary conditions in phase field models of fracture. *PAMM*. 2015;15:155-156. doi:10.1002/pamm.201510068

27. Bryant EC, Sun WC. A mixed-mode phase field fracture model in anisotropic rocks with consistent kinematics. *Comput Methods Appl Mech Eng*. 2018;342:561-584. doi:10.1016/j.cma.2018.08.008

28. Wang Q, Feng YT, Zhou W, Cheng Y, Ma G. A phase-field model for mixed-mode fracture based on a unified tensile fracture criterion. *Comput Methods Appl Mech Eng*. 2020;370:113270. doi:10.1016/j.cma.2020.113270

29. Yue Q, Zhou W, Wang Q, Feng YT, Ma G, Chang X. An adaptive phase-field model based on bilinear elements for tensile-compressive-shear fracture. *Comput Math with Appl*. 2022;105:112-135. doi:10.1016/j.camwa.2021.11.010

30. Steinke C, Kaliske M. A phase-field crack model based on directional stress decomposition. *Comput Mech*. 2019;63:1019-1046. doi:10.1007/s00466-018-1635-0

31. Fan M, Jin Y, Wick T. A quasi-monolithic phase-field description for mixed-mode fracture using predictor–corrector mesh adaptivity. *Eng Comput*. 2021;38:2879-2903. doi:10.1007/s00366-021-01423-6

32. Freddi F, Royer-Carfagni G. Regularized variational theories of fracture: a unified approach. *J Mech Phys Solids*. 2010;58:1154-1174. doi:10.1016/j.jmps.2010.02.010

33. Wu JY, Cervera M. A novel positive/negative projection in energy norm for the damage modeling of quasi-brittle solids. *Int J Solids Struct*. 2018;139-140:250-269. doi:10.1016/j.ijsolstr.2018.02.004

34. Fei F, Choo J. A phase-field method for modeling cracks with frictional contact. *Int J Numer Methods Eng*. 2020;121:740-762. doi:10.1002/nme.6242

35. Fei F, Choo J. A phase-field model of frictional shear fracture in geologic materials. *Comput Methods Appl Mech Eng*. 2023;369:113265. doi:10.1016/j.cma.2020.113265

36. Luo C, Chen L, Huang Y. A phase-field crack model based on a directional strain decomposition and a stress-driven Crack-Opening Indicator. *Comput Methods Appl Mech Eng*. 2021;384:113928. doi:10.1016/j.cma.2021.113928

37. Steinke C, Storm J, Kaliske M. Energetically motivated crack orientation vector for phase-field fracture with a directional split. *Int J Fract*. 2022;237:15-46. doi:10.1007/s10704-022-00633-3

38. Backers T, Stephansson O, Rybacki E. Rock fracture toughness testing in Mode II-punch-through shear test. *Int J Rock Mech Mining Sci*. 2002;39:755-769. https://doi.org10.1016/S1365-1609(02)00066-7

39. Backers T, Dresen G, Rybacki E, Stephansson O. New data on mode II fracture toughness of rock from the punch-through shear test. *Int J Rock Mech Min Sci*. 2004;41:351-352. doi:10.1016/j.ijrmms.2003.12.059

40. Choo J, Sohail A, Fei F, fong Wong T. Shear fracture energies of stiff clays and shales. *Acta Geotech*. 2021;16:2291-2299. doi:10.1007/s11440-021-01145-5

41. Zhang C, Li D, Wang C, Ma J, Zhou A, Xiao P. Effect of confining pressure on shear fracture behavior and surface morphology of granite by the short core in compression test. *Theor Appl Fract Mech*. 2022;121:103506. doi:10.1016/j.tafmec.2022.103506

42. Wu H, Kemeny J, Wu S. Experimental and numerical investigation of the punch-through shear test for mode II fracture toughness determination in rock. *Eng Fract Mech*. 2017;184:59-74. doi:10.1016/j.engfracmech.2017.08.006

43. Fei F, Choo J. Double-phase-field formulation for mixed-mode fracture in rocks. *Comput Methods Appl Mech Eng*. 2021;376:113655. doi:10.1016/j.cma.2020.113655

44. Wu JY, Huang Y. Comprehensive implementations of phase-field damage models in Abaqus. *Theor Appl Fract Mech*. 2020;106:102440. doi:10.1016/j.tafmec.2019.102440

45. Jiang Y, Li C, Wu C, Rabczuk T, Fang J. A double-phase field method for mixed mode crack modelling in 3D elasto-plastic solids with crack-direction-based strain energy decomposition. *Comput Methods Appl Mech Eng*. 2023;405. doi:10.1016/j.cma.2023.115886

46. Wu J. Image-based simulation of complex fracture networks by numerical manifold method. *Int J Numer Methods Eng*. 2021;122:3100-3119. doi:10.1002/nme.6655

47. Wu J. 3D simulation of complex fractures with a simple mesh. *Int J Numer Methods Eng*. 2022;123:3713-3732. doi:10.1002/nme.6986

48. Ambati M, Gerasimov T, de Lorenzis L. A review on phase-field models of brittle fracture and a new fast hybrid formulation. *Comput Mech*. 2015;55:383-405. doi:10.1007/s00466-014-1109-y

49. Samaniego E, Anitescu C, Goswami S, et al. An energy approach to the solution of partial differential equations in computational mechanics via machine learning: concepts, implementation and applications. *Comput Methods Appl Mech Eng*. 2020;362:112790. doi:10.1016/j.cma.2019.112790

50. Goswami S, Anitescu C, Rabczuk T. Adaptive fourth-order phase field analysis using deep energy minimization. *Theor Appl Fract Mech*. 2020;107:102527. doi:10.1016/j.tafmec.2020.102527

51. Ghaffari Motlagh Y, Jimack PK, de Borst R. Deep learning phase-field model for brittle fractures. *Int J Numer Methods Eng*. 2023;124:620-638. doi:10.1002/nme.7135

52. Xu Y, Yao W, Zhao G, Xia K. Evaluation of the short core in compression SCC;method for measuring mode II fracture toughness of rocks. *Eng Fract Mech*. 2020;224. doi:10.1016/j.engfracmech.2019.106747

53. Li D, Zhang C, Zhu Q, Ma J, Gao F. Deformation and fracture behavior of granite by the short core in compression method with 3D digital image correlation. *Fatigue Fract Eng Mater Struct*. 2022;45:425-440. doi:10.1111/ffe.13606

54. Zhang C, Li D, Wang C, Ma J, Zhou A, Xiao P. Effect of confining pressure on shear fracture behavior and surface morphology of granite by the short core in compression test. *Theor Appl Fract Mech*. 2022;121:103506. doi:10.1016/j.tafmec.2022.103506

55. Bobet A, Einstein HH. Numerical modeling of fracture coalescence in a model rock material. *Int J Fract*. 1998;92:221-252.

56. Bobet A, Einstein HH. Fracture coalescence in rock-type materials under uniaxial and biaxial compression. *Int J Rock Mech Min Sci*. 1998;35:863-888. doi:10.1016/S0148-9062(98)00005-9

57. Bobet A. *Fracture Coalescence in Rock Materials: ExpeIilnental Observations and Numerical Predictions*. Massachusetts Institute of Technology; 1997.